Journal of Materials Chemistry A

PAPER

Facile synthesis of mesoporous hierarchical Co_3O_4–TiO_2 p–n heterojunctions with greatly enhanced gas sensing performance

Received 00th January 20xx,
Accepted 00th January 20xx

DOI: 10.1039/x0xx00000x

www.rsc.org/MaterialsA

Jiajun Zhang,[a] Pinggui Tang,*[,a,b,c] Tongyuan Liu,[a] Yongjun Feng,[a] Chris Blackman,[c] and Dianqing Li*[,a,b]

The development of highly active, sensitive and durable gas sensing materials for the detection of volatile organic compounds (VOCs) is extremely desirable in gas sensors. Herein, a series of mesoporous hierarchical Co_3O_4–TiO_2 p–n heterojunctions have been prepared for the first time via the facile thermal conversion of hierarchical CoTi layered double hydroxides (CoTi–LDH) precursors at 300–400 °C. The resulting Co_3O_4–TiO_2 nanocomposites showed superior sensing performance towards toluene and xylene in comparison with Co_3O_4 and TiO_2 at low temperature, and the sample with a Co/Ti molar ratio of 4 shows optimal response (R_g/R_a = 113, R_g and R_a denote the sensor resistance in a target gas and in air, respectively) to 50 ppm xylene at 115 °C. The ultrahigh sensing activity of theses Co_3O_4–TiO_2 p–n heterojunctions originates from their hierarchical structure, high specific surface area (>120 m^2 g^{-1}), and the formation of numerous p–n heterojunctions, which results in full exposure of active sites, easy adsorption of oxygen and target gases, and large modulation of resistance. Importantly, hierarchical Co_3O_4–TiO_2 heterojunctions possess advantages of simple preparation, structural stability, good selectivity and long-term durability. Therefore, this work provides a facile approach for the preparation of hierarchical Co_3O_4–TiO_2 p–n heterojunctions with excellent activity, sensitivity and durability, which can be used as a promising material for the development of high-performance gas sensors.

1. Introduction

Volatile organic compounds (VOCs), such as toluene, xylene, acetone and formaldehyde, are the most common and hazardous indoor air pollutants. For instance, xylene is a harmful organic compound that not only irritates eyes, nose, skin and respiratory system, but also induces serious symptoms such as headaches, fatigue, dizziness, rapid heart rate and unconsciousness even at low concentration.[1, 2] Toluene and xylene come from various materials including building materials, paints, aerosols, disinfectants, air fresheners and automotive parts. Metal oxide semiconductor based gas sensors have attracted considerable attention because of their high portability, simplicity of use and low cost, and have previously been used to realize real-time monitoring of toluene and xylene.[3] However, such systems typically possess disadvantages of low sensitivity and high operating temperature, which hampers the sensitive and long-term detection of toluene and xylene. Therefore, there is a need to develop high-performance gas sensors with high sensitivity, low operating temperature and good stability for real-time monitoring of toluene and xylene.

A variety of metal oxide semiconductors have been used as sensing materials to detect VOCs, such as ZnO,[4-6] SnO_2,[7-9] In_2O_3,[10-12] Co_3O_4,[13-15] TiO_2,[16, 17] WO_3,[18-21] Fe_2O_3,[22-24] Cu_2O/CuO,[25, 26] and NiO.[27] Among these metal oxide semiconductors, Co_3O_4 is believed to be a promising candidate for sensing of toluene and xylene because of its excellent catalytic activity for oxidizing them at low temperature which results from its larger adsorption amount of oxygen[28] on the surface than others and multivalent properties facilitating redox reactions.[29-32] Recently, vast research efforts have been spent on the synthesis of different Co_3O_4 nanostructures such as nanospheres, nanocubes, nanofibers, nanosheets, core-shell structures, etc. for use in gas sensing. Wang et al.[33] prepared Co_3O_4 nanorods through a facile one-pot method followed by calcination at 450 °C and the response of the prepared Co_3O_4 nanorods to 200 ppm toluene reached 35 at the working temperature of 200 °C. Sun et al.[13] synthesized nearly monodisperse Co_3O_4 nanocubes via a microwave-assisted solvothermal process and found that Co_3O_4 nanocubes showed responses of 4.7 and 6.45 to 100 ppm toluene and xylene respectively, at 200 °C. Though Co_3O_4 nanomaterials show a response to toluene and xylene in a wide concentration range, the sensitivity is still very low toward toluene and xylene with concentration lower than 50 ppm and the working temperature is relatively high (above 200 °C), which hinders its practical application in the fields of gas sensors.

[a] State Key Laboratory of Chemical Resource Engineering, Beijing University of Chemical Technology, Beijing 100029, P.R. China.
[b] Beijing Engineering Center for Hierarchical Catalysts, Beijing University of Chemical Technology, Beijing 100029, P.R. China.
[c] Department of Chemistry, University College London, 20 Gordon Street, WC1H0AJ London, UK.

Electronic Supplementary Information (ESI) available. See DOI: 10.1039/x0xx00000x

It is well known that fabrication of hierarchical structures, doping with other metal oxides, modification with noble metals, and formation of heterojunctions are effective ways to enhance the gas sensing performance of metal oxide semiconductors.[5, 27, 33-35] It is worth noting that the formation of p–n heterojunctions is an efficient and cost-effective technique to improve the activity and sensitivity of gas sensors[3, 34, 35], and hierarchical structures offer abundant pores and large surface area which benefit the diffusion and adsorption of testing gases.[26] For example, Deng et al.[16] prepared CuO–TiO_2 heterostructure nanofibers and found that the formation of p–n heterojunctions considerably improved the sensitivity of TiO_2 nanofibers to formaldehyde at 200 ºC. Volanti et al.[26] prepared CuO with urchin-like, fiber-like, and nanorods morphologies and found that urchin-like CuO is most effective for the detection of hydrogen. Nevertheless, the preparations of interconnected and homogenerously distributed p–n heterojunctions with hierarchical structure are rarely reported, and it is still a great challenge to fabricate such p–n heterojunctions.

Layered double hydroxides (LDH) are a class of anionic layered clays which have been intensively studied in the past two decades. LDH have a general formula of $[M_{1-x}^{2+}M_x^{3+}(OH)_2]^{x+}(A^{n-})_{x/n}\cdot mH_2O$, where x is usually in the range of 0.2–0.33, M^{2+} and M^{3+} represent various di- and trivalent metal cations in the LDH host sheets, and A^{n-} is the interlayer guest anion. The positively charged host metal hydroxide layers and negatively charged guest anions are combined through weak interactions. In some cases, M^{3+} can be replaced by M^{4+}, forming a unique kind of LDH. Much attention has been paid to LDH because of their adjustable chemical composition, anion exchange ability, tunable charge density, and multi-funtionalities, and they have been widely used in the fields of catalysis, optics, electrochemistry, adsorption, anion exchange, and polymer additives.[36-40] LDH have already been used as precursors to prepare different kinds of mixed metal oxides,[41-43] however, to the best of our knowledge, they are seldom adopted to fabricate p–n heterojunctions.

Herein, mesoporous hierarchical Co_3O_4–TiO_2 p–n heterojunctions are fabricated through a facile precursor route. Hierarchical CoTi–LDHs were first prepared by a new co-precipitation method, followed by calcination at 300–400 ºC to form Co_3O_4–TiO_2 heterojunctions. The gas sensing performance was systematically studied, and it was found that the Co_3O_4–TiO_2 heterojunctions showed superior sensing performance towards toluene and xylene compared with Co_3O_4 and TiO_2 at low temperature (115 ºC), as a result of the hierarchical structure, high specific surface area (>120 $m^2\ g^{-1}$) as well as the formation of p–n heterojunctions. Moreover, Co_3O_4–TiO_2 heterojunctions displayed the merits of simple preparation, structural stability and long-term durability. Therefore, this work provides a facile route for the preparation of hierarchical Co_3O_4–TiO_2 p–n heterojunctions with high sensing response at relatively low operating temperature, which can be used as a promising material for the development of high-performance gas sensors towards VOCs.

2. Experimental

2.1. Materials

All the chemical reagents including cobalt nitrate ($Co(NO_3)_2\cdot 6H_2O$, Tianjin Fuchen Chemical Reagent Factory), titanium tetrachloride ($TiCl_4$, Tianjin Fuchen Chemical Reagent Factory), hydrochloric acid (HCl, 37 w%, Beijing Chemical Factory), salicylic acid ($C_7H_6O_3$, Tianjin Guangfu Fine Chemical Research Institute), urea (Beijing Tongguang Fine Chemical Company) and ethanol (Beijing Chemical Factory) used in the experiments were of analytical grade and were used without further purification. Deionized water with an electrical conductivity of less than 10^{-6} S cm^{-1} was used throughout the experiments.

2.2. Synthesis of CoTi–LDH precursors

A series of CoTi–LDH precursors with different Co/Ti molar ratios were prepared by co-precipitation of cobalt and titanium salts from homogeneous solution in the presence of salicylic acid. In a typical synthesis, a solution (150 mL) of $Co(NO_3)_2$ (0.016 mol), $TiCl_4$ (0.004 mol) and salicylic acid (0.01 mol) were mixed with urea solution (0.2 mol, 50 mL) under vigorous stirring. The $TiCl_4$ solution was prepared by dissolving liquid $TiCl_4$ in concentrated HCl solution, cooled in an ice bath, with the volume ratio of $TiCl_4$/HCl set to 1. The resulting solution was then heated to 95 ºC and maintained for 24 h with stirring. The obtained precipitate was centrifuged and washed five times with deionized water and once with anhydrous ethanol, and then dried in an oven at 60 ºC for 12 h. CoTi–LDH precursors with different Co/Ti molar ratios, pure TiO_2 and layered cobalt hydroxide (Co–LH) were synthesized according to the same process above by changing the molar amounts of $Co(NO_3)_2$ and $TiCl_4$ but keeping their total molar amount to be 0.02 mol. The amounts of materials used for precursor synthesis are listed in Table 1. The resulting CoTi–LDH precursors in this stage are denoted as CoTi–LDH–x (x= 2, 3, 4, and 10, indicating the Co/Ti molar ratio used in the preparation process).

2.3. Preparation of Co_3O_4–TiO_2 p–n heterojunctions

Co_3O_4–TiO_2 p–n heterojunctions were prepared by calcining the as-synthesized CoTi–LDH precursors at the given temperature. Typically, the powders of CoTi–LDH precursors

Table 1 detailed preparation condition of the precursors

Sample	$Co(NO_3)_2\cdot 6H_2O$	$TiCl_4$	HCl (37 w%)
CoTi-LDH-2	0.0133 mol	0.0067 mol	730 µl
CoTi-LDH-3	0.015 mol	0.005 mol	550 µl
CoTi-LDH-4	0.016 mol	0.004 mol	440 µl
CoTi-LDH-10	0.0182 mol	0.0018 mol	200 µl
Co-LH	0.02 mol	-	-
TiO_2	-	0.02 mol	2200 µl

were placed in ceramic boats and transferred into a temperature-programmed furnace with a heating rate of 5 °C min^{-1}, and calcined at 300, 350 or 400 °C for 4 h in air atmosphere. The final products are denoted as CoTiO–x–T (x = 2, 3, 4, and 10; T = 300, 350, and 400), where x and T represent theoretical Co/Ti molar ratio of CoTi–LDH precursor and the calcining temperature, respectively. Pure TiO_2 and Co_3O_4 powder were also obtained by calcining the synthesized TiO_2 and Co–LH precursor according to the same procedure at 350 °C.

2.4. Characterization

The crystal phases of the samples were analyzed by X–ray diffraction on a Rigaku D/max–Ultima III X–ray powder diffractometer using Ni–filtered Cu Kα radiation at 45 kV and 40 mA, with a scan speed of 10° min^{-1} and a scan range from 3 to 70°. Surface morphology and element contents of the sample were investigated on a field-emission scanning electron microscope (SEM; Zeiss Supra 55) operated at a voltage of 20 kV equipped with an energy-dispersive X-ray spectrometer (EDX). Transmission electron microscope (TEM; Hitachi H–800) and high resolution transmission electron microscope (HRTEM, JEOL JEM–2010 with an accelerating voltage of 200 kV) were employed to observe the morphology and structure of the samples. The decomposition characteristics of the LDH precursor were investigated using thermogravimetric (TG) and differential thermal (DTA) analyses, which were carried out in air on a PCT-IA thermal analyzer with a heating rate of 5 °C min^{-1}. The specific surface area and pore volume of the samples were measured by a nitrogen adsorption–desorption system (Micromeritics Surface Area and Porosity Gemini VII 2390 system) through Brunauer-Emmett-Teller (BET) and Barrett–Joyner–Halenda (BJH) methods, respectively. All the samples were degassed at 200 °C for 8 h prior to the measurements. The surface elemental compositions analysis was performed using an ESCALAB 250 X–ray photoelectron spectrometer with Al Kα as the excitation source (XPS).

2.5. Gas sensing test

The as-prepared powders were ground and mixed with ethanol to form a paste, which was then coated on the surface of an alumina tube substrate (4 mm in length, 1.2 and 0.8 mm in external and internal diameters, and previously attached with a pair of gold electrodes) to form a film. A Ni–Cr heating wire was then inserted into the tube to serve as a heater and control the heating temperature by tuning the heating current. The fabricated gas sensors were heated at 250 °C for 24 hours in a furnace to stabilize the sensor before gas sensing tests. The gas-sensing performances of the samples were performed on the CGS–8 intelligent gas sensing analysis system (Elite Tech Co., Ltd.) under laboratory conditions (Temperature: 25–35 °C, Relative humidity: 20–35%). The schematic diagram of analysis system and experimental process were illustrated in previous reports.[44] The gas response of the sensor to a reducing gas was defined as R_g/R_a for a p-type semiconductor, where R_g and R_a denote the resistances of the sensor in the analyte gas and in air, respectively.[45] The response and recovery times are defined as the time taken by sensors to achieve 90% of the steady-state resistance changes in the case of adsorption and desorption of testing gas, respectively.

Results and discussion

3.1. Structure, morphology and composition

The crystalline phase structures of the as-synthesized precursors and the corresponding calcined products were examined by XRD. In the XRD patterns of the as-synthesized LDH precursors (Fig. 1a), all of the diffraction peaks are in good agreement with the characteristic peaks of LDH-like materials.[46] A series of basic reflections such as (003), (006) and (009) appear at 2θ value of 6.98，14.06 and 21.39, corresponding to lattice spacing of 1.26，0.63 and 0.42 nm, respectively. By subtracting the layer thickness of 0.48 nm from the basal spacing (d_{003}), the gallery height is about 0.78 nm for each CoTi–LDH, which is larger than the size of salicylic anion (0.63 nm, as shown in Fig. S1 in the supporting information), indicating the successful intercalation of salicylic anions into the interlayer of CoTi–LDH. It is worth noting that only the reflections of LDH-like materials are observed without any other reflections, indicating the high purity of the LDH precursor. After calcination at 350 °C for 4 h, a series of new reflections appear (Fig. 1b), which are in good agreement with the standard reflections of Co_3O_4 (JCPDS card No. 43–1003), suggesting the complete conversion of as-synthesized LDH precursors to oxides by calcination. No obvious peaks related to TiO_2 were found in the XRD patterns of the Co_3O_4–TiO_2 nanocomposites, probably owing to the low crystallinity and relatively low content of TiO_2 in the nanocomposites.

In comparison with the pure Co_3O_4 sample, the diffraction peaks of Co_3O_4–TiO_2 nanocomposites are relatively low, indicating the lower crystallinity of Co_3O_4–TiO_2 nanocomposites. The reflection intensity of the Co_3O_4–TiO_2 nanocomposites increases with the increase of Co_3O_4 content in the composite. The average crystal sizes of CoTiO–2–350, CoTiO–3–350, CoTiO–4–350, CoTiO–10–350 and pure Co_3O_4 calculated from the Scherrer formula are 13, 14, 14, 15 and 16

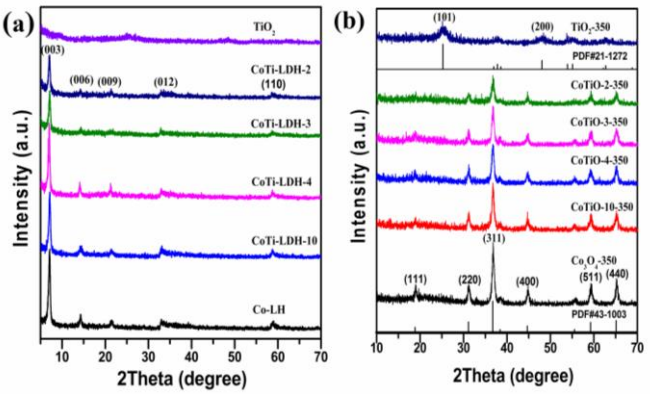

Fig. 1 XRD patterns of (a) the as-synthesized precursors, and (b) the calcined products.

nm, respectively, suggesting the average crystal size of Co_3O_4–TiO_2 nanocomposites is smaller than that of Co_3O_4, which is helpful to improve the gas sensing performance of materials.

The morphology of Co–LH, CoTi–LDH and TiO_2 precursors, and their calcination products was characterized by SEM, which is displayed in Fig. 2 and Fig. S2 in the supporting information. Typical morphology of the as-prepared CoTi–LDH precursors is shown in Fig. 2a, c, e, and g. The synthesized precursors are composed of very thin flakes with size of several hundred nanometers and thickness of 10–20 nm, forming three dimensional hierarchical structures. By calcining these CoTi–LDH precursors at 350 ℃ for 4 h, black powders of Co_3O_4–TiO_2 nanocomposites were prepared, and the typical morphology is shown in Fig. 2b, d, f, and h. Evidently, the calcined products retain the flake and hierarchical structures of the LDH precursors, indicating the stability of the hierarchical structures.

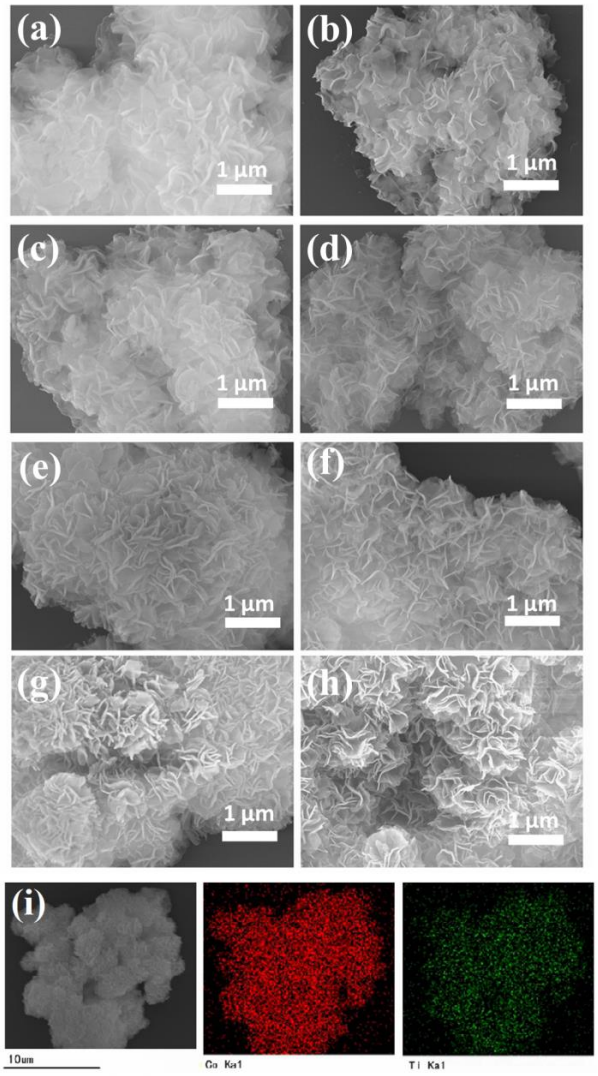

Fig. 2 SEM images of LDH precursors: (a) CoTi–LDH–2, (c) CoTi–LDH–3, (e) CoTi–LDH–4, (g) CoTi–LDH–10, and their corresponding calcined products: (b) CoTiO–2–350, (d) CoTiO–3–350, (f) CoTiO–4–350, (h) CoTiO–10–350; and (i) SEM image with EDS mapping of CoTiO–4–350.

The element contents and distribution of CoTiO–4–350 were investigated by EDX, and the results shown in Fig. S3 in the supporting information reveal that Co and Ti are present in the nanocomposites and the molar percent of Ti is about 18%, which is near the theoretical molar content of Ti (20%). The lower content of Ti in the composite may result from the loss of $TiCl_4$ in the preparation of $TiCl_4$ solution due to its high volatility. EDS elemental mapping was conducted to identify the spatial distribution of Co and Ti in the CoTiO–4–350 nanocomposites. The obtained results (Fig. 2i) unambiguously confirm that Co and Ti elements are uniformly distributed in the composites, which implies the generation of Co_3O_4–TiO_2 p–n heterojunctions.

In order to further study the internal structure of CoTiO–4–350 nanocomposites in more detail and clearly demonstrate the formation of Co_3O_4–TiO_2 p–n heterojunctions, TEM and HRTEM characterizations were performed on the sample of CoTiO–4–350 (Fig. 3). Fig. 3a shows a typical TEM image of CoTiO–4–350, in which thin flakes were found. As shown in Fig. 3b, c and d, the interfaces between Co_3O_4 and TiO_2 nanoparticles are clearly observed, and the lattice fringes of CoTiO–4–350 display lattice spacing of 0.466 nm, 0.286 nm and 0.237 nm in the particles, which match well with the (111) and (220) planes of the Co_3O_4 and (004) plane of TiO_2, respectively. Therefore, highly uniform Co_3O_4–TiO_2 p–n heterojunctions are derived by calcining CoTi–LDH precursors at appropriate temperatures.

The decomposition behavior of CoTi–LDH–4 was characterized by using TG and DTA analysis. As displayed in Fig. 4, there exists two obvious mass loss steps in the TG curve: the first one from room temperature to 230 ℃ with a mass loss of 13% can be attributed to the elimination of physical absorbed

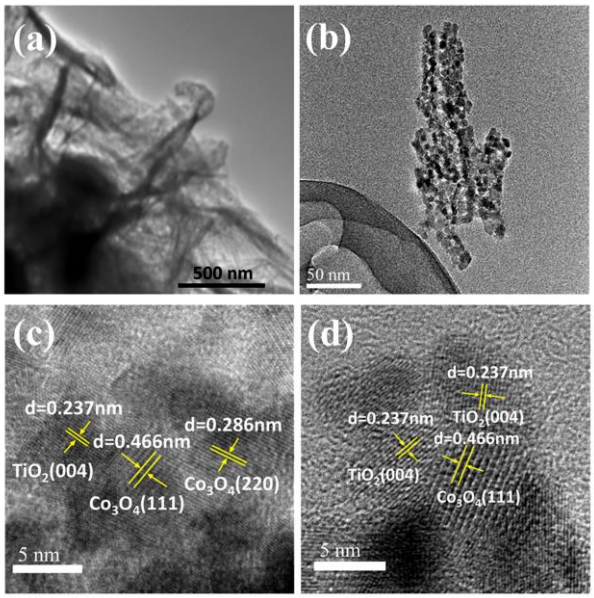

Fig. 3 TEM image (a) and HRTEM images (b, c and d) of CoTiO–4–350.

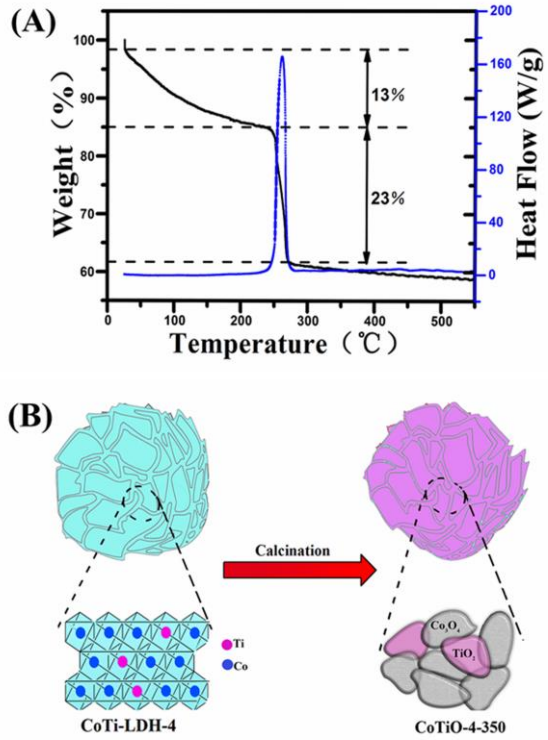

Fig. 4 (a) TG and DTA curves of the CoTi–LDH–4, and (b) schematic illustration of the formation of Co_3O_4–TiO_2 p–n heterojunctions from CoTi–LDH–4 precursor.

water, interlayer water and the dehydroxylation of the LDH layers; the second one starting from 230 ºC to 300 ºC with a sharp mass loss of about 23% is due to the oxidative thermal decomposition of salicylic anions in the interlayer of CoTi–LDH. Accordingly there is a predominantly endothermic peak centered at 255 ºC in the DTA curve, further confirming the oxidative thermal decomposition of salicylic anions. Such a large mass loss signifies that large amounts of H_2O and CO_2 will be released in the decomposition process of CoTi–LDH–4 precursor, leaving lots of pores in the decomposition products. Only a small amount of mass loss is observed in the range of 300–550 ºC, which may be ascribed to the oxidation for decomposition residue of salicylic anions. Thus, in order to improve the stability of the gas sensor for a long-term application, all Co_3O_4–TiO_2 nanocomposites were prepared by annealing the precursors at no lower than 300 ºC.

The nitrogen adsorption-desorption isotherms were measured to investigate the specific surface area and the pore structure of the obtained products, which are shown in Fig. 5 and Fig. S4 in the supporting information. The specific surface areas of CoTiO–2–350, CoTiO–3–350, CoTiO–4–350, and CoTiO–10–350 calculated by the BET method are 128, 124, 122, and 95 $m^2\ g^{-1}$, respectively, which is considerably larger than that of Co_3O_4–350 (61 $m^2\ g^{-1}$). Such a high specific surface area is expected to be favourable for the improvement of the gas sensing performance of Co_3O_4 based materials. The specific surface area decreases a little with the increase of the Co/Ti molar ratio from 2 to 4, but decreases significantly when the

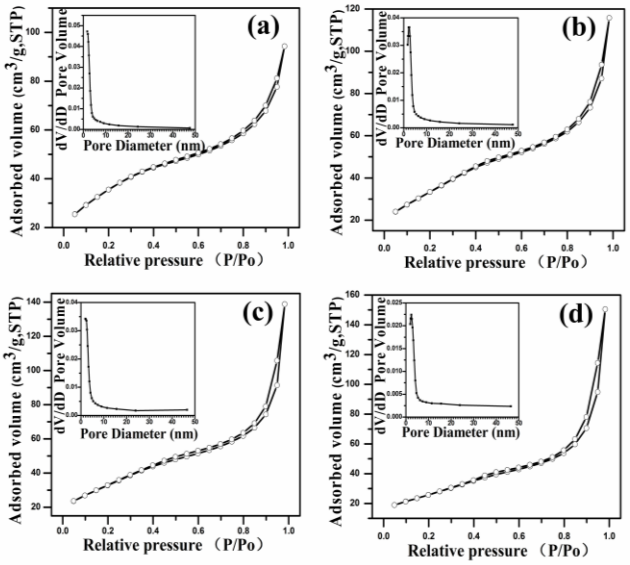

Fig. 5 Nitrogen adsorption-desorption isotherms and pore size distribution of (a) CoTiO–2–350 (b) CoTiO–3–350, (c) CoTiO–4–350, and (d) CoTiO–10–350.

molar ratio increases to 10. All of the samples show a typical III adsorption isotherm with H3–type hysteresis loops at a relative pressure of 0.75–0.95, suggesting the presence of ample mesopores. Moreover, the pore size distribution curves obtained by the BJH method also show that pore size of Co_3O_4–TiO_2 nanocomposites is mainly in the range of 2–50 nm and the majority of pores are in size of 2–4 nm. For Co_3O_4 the amounts of pores in size of 2–4 nm are markedly lower than those of Co_3O_4–TiO_2 nanocomposites. As a result, the specific surface area of Co_3O_4–350 is significantly lower than that of Co_3O_4–TiO_2 nanocomposites.

The effects of calcination temperature on the specific surfaces, pore size distribution, and crystalline phase structures are also investigated. The nitrogen adsorption-desorption isotherms and pore size distribution of CoTiO–4–300 and CoTiO–4–400 are shown in Fig. S5 in the supporting information. The results show that the specific surface area of Co_3O_4–TiO_2 nanocomposites decreases and the average pore size increases from 7.1 to 9.9 and 27 nm as the calcination temperature increases from 300 to 350 and 400 ºC. As shown in Fig. S6 in the supporting information, only reflections of Co_3O_4 phase are present in all calcined products, indicating the calcination temperature has little influence on the phase structure in the range of 300–400 ºC. However, the intensity of the peaks increases as the calcination temperature increases, suggesting better crystallinity is achieved at higher calcination temperature.

XPS measurement was carried out to study the chemical composition and chemical states of elements of Co_3O_4–350 and CoTiO–4–350, and the results are displayed in Fig. 6.

During the XPS analysis, the C 1s peak located at 284.6 eV was selected as the reference. Four elements (Co, O, Ti and C) are identified from the full-survey-scan spectrum of CoTiO–4–350

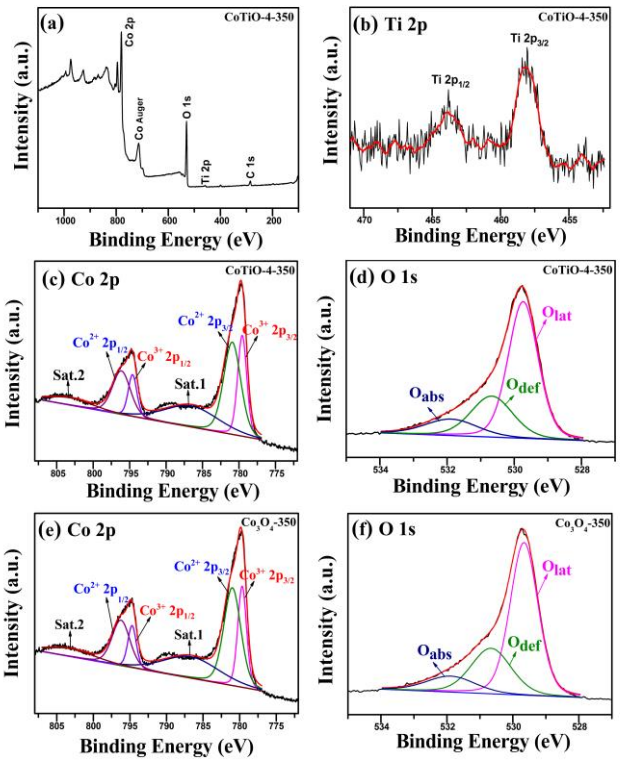

Fig. 6 XPS spectra of the CoTiO–4–350 (a) and an enlarged spectra of Ti 2p (b), Co 2p (c) O 1s (d); and the Co 2p (e), O 1s (f) spectra of pure Co_3O_4–350.

(Fig. 6a) and no peaks of other elements are observed, indicating high purity of the synthesized nanocomposites. As shown in Fig. 6b, the peaks appearing at 458.1 eV and 463.8 eV were ascribed to the Ti $2p_{3/2}$ and Ti $2p_{1/2}$ spin-orbit peaks for a typical TiO_2. The two strong peaks located at 779.6 eV and 794.7 eV (Fig. 6c) correspond to Co $2p_{3/2}$ and Co $2p_{1/2}$ spin-orbit peaks of Co_3O_4. The fitting peak at 779.5 eV is attributed to Co^{3+} $2p_{3/2}$ spin-orbit peak, while the fitting peak at 780.9 eV is due to Co^{2+} $2p_{3/2}$ spin-orbit peak. It should be noted that a weak satellite peak at 786.6 eV beside the position of the main peak of Co $2p_{3/2}$ is obviously observed in the spectra, suggesting the existence of Co_3O_4 phase. The XPS spectra of CoTiO–4–350 further confirms that the as-prepared sample is a composite of Co_3O_4 and TiO_2. Compared with the Co 2p peaks of pure Co_3O_4, the Co 2p peaks of CoTiO–4–350 slightly shift to lower binding energy, which indicates that there may exist electron transfer between Co_3O_4 and TiO_2.

As shown in Fig. 6d, f and Fig. S7 in the supporting information, there are also some slight differences between O 1s XPS peaks of Co_3O_4–350 and Co_3O_4–TiO_2 nanocomposites. The asymmetric O 1s peak can be coherently fitted into three components (O_{lat}, O_{def}, O_{abs},). The O_{lat} component of O 1s spectra centered at 529.7 eV is attributed to O^{2-} ions in the lattice of Co_3O_4–350 and CoTiO–4–350, the middle one (O_{def}) located at 530.7 eV is assigned to O^{2-} ions in oxygen deficient regions within the matrix, and the O_{abs} component at around 531.9 eV is usually attributed to chemisorbed and dissociated oxygen species (O^{2-}, O_2^-, or O^-) and OH^-. Table 2 and Table S1 summarize the relative percentage of oxygen species on the surface of Co_3O_4–350, CoTiO–2–350, CoTiO–3–350, CoTiO–4–350 and CoTiO–10–350. It clearly demonstrates that the relative percentages of O_{lat} and O_{def} components of CoTiO–2–350, CoTiO–3–350, CoTiO–4–350 and CoTiO–10–350. are lower than those of Co_3O_4–350; on the contrary, the relative percentage of O_{abs} of CoTiO–2–350 (12.1%), CoTiO–3–350 (12.4%), CoTiO–4–350 (13.0 %) and CoTiO–10–350 (11.9%) is higher than that of Co_3O_4–350 (11.4 %). Obviously, Co_3O_4–TiO_2 nanocomposites with much larger specific surface area are able to generate more oxygen species than Co_3O_4–350, which undoubtly can enhance the gas sensing performance.

3.2. Gas sensing performance

To evaluate the influence of composition on the sensitivity of Co_3O_4–TiO_2 p–n heterojunctions and to find out the optimal operating temperature, the sensing tests of the sensors based on Co_3O_4, TiO_2 and Co_3O_4–TiO_2 p–n heterojunctions with different Co/Ti molar ratios calcined at 350 °C to 50 ppm xylene gas were carried out at different operating temperatures ranging from 60 to 135 °C. As shown in Fig. 7a and Table S2 in the supporting information, TiO_2 shows no response to 50 ppm xylene at the temperature range of 60–135 °C, but Co_3O_4 and Co_3O_4–TiO_2 p–n heterojunctions are very sensitive to xylene. The highest responses of Co_3O_4–TiO_2 p–n nanocomposites are considerably larger than that of Co_3O_4, indicating the formation of Co_3O_4–TiO_2 p–n heterojunctions significantly enhances the sensitivity of Co_3O_4. The response increases from 43 for Co_3O_4 to 63 for CoTiO–10–350 when the molar ratio of Ti/Co increases from 0 to 0.1, and further sharply rises to 130 as the Ti/Co molar ratio rises to 0.25. However, a further increase of Ti/Co molar ratio to 0.33 and 0.50 will lead to the decrease of response. Therefore, CoTiO–4–350 with a Ti/Co molar ratio of 0.25 displayed the highest response, indicating that the TiO_2 content in hierarchical Co_3O_4–TiO_2 p–n heterojunctions should be optimized to obtain the best sensing properties.

In addition, the sensing responses of Co_3O_4 and Co_3O_4–TiO_2 p–n heterojunctions gradually increase to their maximum values and then decreases afterwards with the continuing rise

Table 2 Results of XPS spectra of pure Co_3O_4–350 and CoTiO–4–350

Samples		Co^{3+} $p_{3/2}$	Co^{2+} $p_{3/2}$	Co^{3+} $p_{1/2}$	Co^{2+} $p_{1/2}$	O_{lat}	O_{def}	O_{abs}
Co_3O_4–350	Binding energy (eV)	779.7	781.0	794.7	796.2	529.7	530.7	531.9
	Relative percentage (%)					62	26.6	11.4
CoTiO–4–350	Binding energy (eV)	779.6	780.9	794.6	796.1	529.7	530.7	531.9
	Relative percentage (%)					61.3	25.7	13

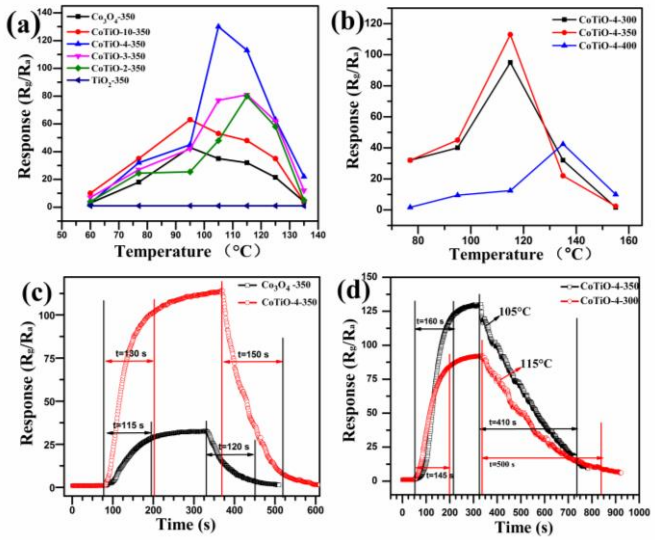

Fig. 7 (a) Response of different sensors to 50 ppm xylene at different operating temperatures; (b) Response of sensors based on CoTiO–4 prepared at different calcinations temperature to 50 ppm xylene; (c) Typical response and recovery curve of Co_3O_4–350 and CoTiO–4–350 to 50 ppm xylene at 115 °C; (d) Typical response and recovery curve of CoTiO–4–350 to 50 ppm xylene at 105 °C and CoTiO–4–300 to 50 ppm xylene at 115 °C.

of operating temperature. Co_3O_4–350, CoTiO–10–350, CoTiO–4–350, CoTiO–3–350 and CoTiO–2–350 reach maximum values at 95, 95, 105, 115, and 115 °C, respectively. Evidently, there is an increasing tendency for the optimal temperature with the increase of Ti molar percentage due to the inactivity of TiO_2. The effect of temperature on the sensor response can be explained as follows: The sensing process of metal oxides semiconductor involves the adsorption of oxygen in air and reaction of the oxygen species and testing gases on the surface-active sites of the material. When the operating temperature is too low, the response is very low because insufficient thermal energy is supplied to overcome the activation energy barrier of chemisorption and surface reaction. However, once the operating temperature increases too much, some adsorbed gas molecules desorb from the surface of metal oxide before reaction, leading to the decrease of response. Therefore, the response reaches maximum at the optimal temperature at which the amount of reacted gases on the surface of the material reaches maximum.

The calcination temperature plays an important role in constructing the structure of metal oxide semiconductors, which is a key factor to determine the performance of gas sensors. The sensing responses of CoTiO–4 obtained at different calcination temperatures (300, 350, and 400 °C) to 50 ppm xylene at different temperatures are tested to ascertain the optimal calcination temperature. As shown in Fig. 7b, the CoTiO–4–350 displayed the highest sensitivity at 105 °C among the three samples. Hence, 350 °C can be considered as the optimal calcination temperature. Moreover, it should be noted that CoTiO–4–350 showed a response of 113 to 50 ppm xylene at 115 °C, which is just slightly lower than the response of 130 at 105 °C. Nevertheless, as shown in Fig. 7c and d, the response and recovery times of CoTiO–4–350 at 105 °C are about 160 and 410 s, respectively, which are considerably larger than those at 115 °C. The temperature of 115 °C is thereby chosen as the optimal operating temperature for CoTiO–4–350 and adopted for other tests.

The response characteristic curves of Co_3O_4–350 and CoTiO–4–350 to 50 ppm xylene at 115 °C shown in Fig. 7c clearly show that the response of CoTiO–4–350 (113) is noticeably higher than that of Co_3O_4–350 (32), demonstrating that the formation of Co_3O_4–TiO_2 p–n heterojunctions can effectively improve the gas sensing ability. The response and recovery times of CoTiO–4–350 are 130 s and 150 s, corresponding to the times taken for reaching 90% of the total resistance change values after injecting or removing of xylene, respectively, which are slightly longer than those of Co_3O_4–350 (115 and 120 s, respectively). As shown in Fig. 7d, the recovery time for CoTiO-4-300 at 115 °C is about 500 s. The considerably slow recovery may be ascribed to the existence of more small pores in CoTiO-4-300 than CoTiO-4-350 resulting from the lower calcination temperature for CoTiO-4-300.

The dynamic sensing characteristics of CoTiO–4–350 sensor were investigated by exposing it to different concentrations of xylene gas (from 5 ppm to 150 ppm) at the operating temperature of 115 °C. As shown in Fig. 8a, the response of CoTiO–4–350 initially increases with increasing xylene gas concentration, reaching the maximum value at approximately 50 ppm, and is then constant when the concentration is above 50 ppm, indicating that all the active sites may be occupied by xylene molecules at 50 ppm and above. It is evident that the response and recovery times to xylene with low concentrations are much longer than those to xylene with high concentrations (above 50 ppm), which may result from the very slow diffusion speed of xylene molecules to the active site at low concentration. Moreover, the inset in Fig. 8a further demonstrates that the response of CoTiO–4–350 increases almost linearly in the range of 5–25 ppm, and the response to xylene is very high in this range, indicating that CoTiO–4–350 is sensitive to xylene and can be used to detect xylene at relatively low concentration. Fig. 8b shows the repeatability of CoTiO–4–350 to 50 ppm xylene at 115 °C. The response and recovery processes during the test demonstrate that CoTiO–4–350 has good sensing reproducibility.

A better selectivity endows the sensor with relatively enhanced response to a certain target gas. Therefore, the gas sensing responses of pure Co_3O_4–350 and CoTiO–4–350 to 50 ppm xylene, toluene, acetone, ethanol, methanol, ammonia, and formaldehyde are tested at 115 °C and the corresponding results are presented in Fig. 8c. It can be seen that the sensor based on CoTiO–4–350 exhibits a higher response than pure Co_3O_4–350. The responses of CoTiO–4–350 to xylene, toluene, acetone, ethanol, methanol, ammonia, and formaldehyde were about 113, 55, 42, 26, 5.8, 4, and 2.8, respectively, while the responses of pure Co_3O_4–350 were about 32, 22, 7.9, 7.3, 2.4, 2, and 1.7, respectively. The responses of CoTiO–4–350 to xylene is 3.5 times higher than that of Co_3O_4–350, further

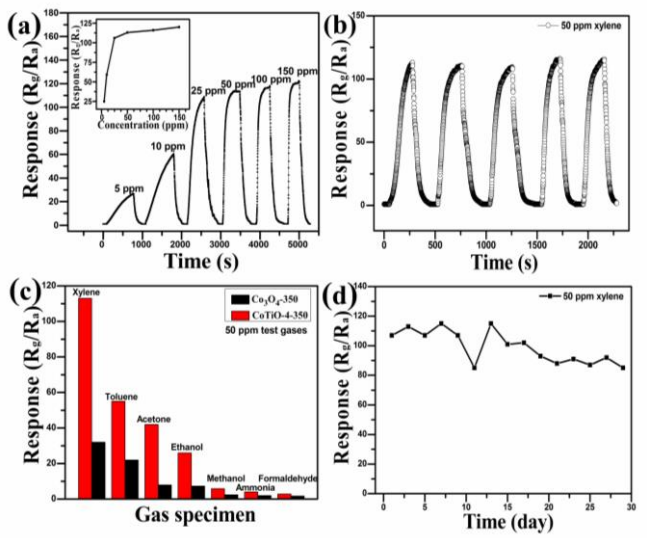

Fig. 8 (a) Dynamic sensing curve and sensing response (inset) of CoTiO–4–350 sensor to a series concentrations of xylene at 115 °C; (b)The response repeatability curve of CoTiO–4–350 to 50 ppm xylene at 115 °C; (c) Response of Co_3O_4–350 and CoTiO–4–350 to 50 ppm various gases at 115 °C; (d) The response stability curve of CoTiO–4–350 to 50 ppm xylene at 115 °C.

Table 3 Sensing performance of varied Co_3O_4 based materials

Materials	Response (R_g/R_a)	Concentration (ppm)	T (°C)	Ref
Co_3O_4 nanocubes	4.7 (toluene) 6.45 (xylene)	100 100	200	13
Cr-doped Co_3O_4 nanorods	25 (xylene)	5	275	14
Co_3O_4 nanofibers	11 (xylene)	100	255	45
Cu_2O–Co_3O_4 core–shell composites	5.4 (xylene)	100	350	47
Co_3O_4–SnO_2 hollow heteronanost-ructures	7.0 (toluene) 18.6 (xylene)	5 5	275	3
Pompon-like Cr-Co_3O_4	6.38 (xylene)	5	139	48
Mesoporous Co_3O_4	23.55 (toluene)	100	190	49
Co_3O_4 concave nanocubes	1.4 (toluene)	200	300	28
Co_3O_4 nanorods	35 (xylene)	200	200	33
Mesoporous Co_3O_4/TiO_2 heterojunction	55 (toluene) 113 (xylene) 25 (xylene)	50 50 5	115	This work

indicating that the formation of Co_3O_4–TiO_2 p–n heterojunctions is an effective way to enhance the gas sensing sensitivity. The response of CoTiO–4–350 to xylene is about 2.7, 4.3, 19.5, 28.3, and 40.4 times higher than that to acetone, ethanol, methanol, ammonia, and formaldehyde, respectively, suggesting the good selectivity of Co_3O_4–TiO_2 p–n heterojunction to xylene. Interestingly, CoTiO–4–350 also shows very high response to toluene (Fig. S9 in the supporting information), which is 2.5 times higher than that of Co_3O_4. It is well known that the sensing process is associated with the adsorption and reaction of gas molecules on the surface of sensing materials. On one hand, the molecular weight of xylene/toluene is larger than that of acetone, ethanol, methanol, ammonia, or formaldehyde, which will promote the adsorption of xylene/toluene on the surfaces of CoTiO–4–350. On the other hand, the reaction between xylene/toluene molecule and reactive oxygen species can release more electrons than other five gas molecules, resulting in much higher response to xylene/toluene than other five gases. Hence, Co_3O_4–TiO_2 p–n heterojunction is a promising material for the sensing of benzene derivatives (xylene and toluene). The stability of the sensor is extremely important for the practical application. Through 15 times tests in 29 days, the response of sensor maintains at around 90 after testing for 29 days as shown in Fig. 8d, indicating that CoTiO–4–350 has good stability.

To date, a variety of Co_3O_4 based materials have been developed to detect xylene and toluene (Table 3). Although several articles have revealed a very high response at a temperature higher than 250 °C, it is not common to fabricate sensors operating at a low temperature of 115 °C or below. For xylene gas, the sensors fabricated from Cr-doped Co_3O_4 nanorods[14] and Co_3O_4–SnO_2 hollow heteronanostructures[3] showed sensing responses of 25 and 18.6 to 5 ppm xylene at 275 °C, respectively. Recently, Zhang's group prepared nanoparticles-assembled hierarchical Co_3O_4 nanorods and reported a response of 35 to 200 ppm xylene at 200 °C.[33] Furthermore, several researchers have reported sensing performance of Co_3O_4 based materials to toluene. The Co_3O_4 nanocubes showed a sensing response of 4.7 to 100 ppm toluene at 200 °C,[13] whereas the mesoporous Co_3O_4 exhibited a sensing response of 23.55 at 190 °C.[49] However, there have been few reports on Co_3O_4 based sensors with a high sensitivity at low operating temperature. Li et al.[48] reported that pompon-like Cr-Co_3O_4 showed responses of 6.38 and about 15 to 5 and 50 ppm xylene at 139 °C, respectively. Obviously, these responses are markedly lower than the responses of 25 and 110 to 5 ppm and 25 ppm xylene obtained by the present work, respectively. Therefore, mesoporous hierarchical Co_3O_4–TiO_2 p–n heterojunctions derived from LDH precursors are superior to previous materials based on Co_3O_4, paving the way to the development of gas sensors working at low temperature.

3.3. Gas Sensing Mechanism

The sensing mechanism of metal oxide semiconductor, which could be explained using the surface-control model, is based

on the change in resistance of the metal oxide during the adsorption and reaction processes of gas molecules on the surface of metal oxide. Fig. 9a shows schematically the formation of depletion layer in the surface region of Co_3O_4 and TiO_2 particles and the corresponding energy band diagram in vacuum. A thin depletion layer forms in the surface region of particle and small band bending occurs near the surface as a result of carrier trapping by surface states. Co_3O_4–Co_3O_4 p–p homojunction and Co_3O_4–TiO_2 p–n heterojunction are formed when the particles are in contact with each other (Fig. 9b), and electrons transfer from n-type semiconductor TiO_2 to p-type semiconductor Co_3O_4 while the holes flow in the opposite direction until the Fermi energy level of them becomes equal, leading to the formation of a self-built electric field in Co_3O_4–TiO_2 p–n heterojunction. Moreover, a depletion layer forms as well in the interface region of Co_3O_4–TiO_2 heterojunction due to recombination of holes in the Co_3O_4 nanoparticle and electrons in the TiO_2 nanoparticle, resulting in band bending at the interface region.

Upon exposure to air, oxygen molecules are adsorbed onto the surface of semiconductor metal oxides, forming ions of O_2^- (below 150 °C), O^- (150–400 °C) and O^{2-} (above 400 °C) through trapping electrons from the conduction band.[35] As the sensing tests were carried out at 115 °C in this study, highly reactive oxygen species of O_2^-(ads) ions may be predominately formed on the surface of p–type Co_3O_4 by capturing electrons from conduction band, and holes are generated at the valence band of Co_3O_4 according to equation 2, resulting in the formation of a hole accumulation layer in the surface region of Co_3O_4 nanoparticle.[33] On the other hand, upon exposure to air, oxygen molecules are adsorbed onto the surface of n–type TiO_2 nanoparticle as well and transform into O_2^-(ads) ions by capturing electrons from TiO_2 conduction band according to equation 3, leading to a thicker electron depletion layer in the surface region of TiO_2 (Fig. 9c).[50] Therefore, the resistance of Co_3O_4 nanoparticle decreases while the the resistance of TiO_2 nanoparticle increases.

$$O_2(g) \longrightarrow O_2(ads) \quad (1)$$

$$O_2(ads) \longrightarrow O_2^-(ads) + h^+ \quad (2)$$

$$O_2(ads) + e^- \longrightarrow O_2^-(ads) \quad (3)$$

Upon exposure to xylene (Fig. 9d), for the Co_3O_4 nanoparticles, xylene molecules are adsorbed onto the surface of Co_3O_4 nanoparticles and then react with the adsorbed oxygen species (O_2^-(ads)) on the surface and will generate CO_2, H_2O and free electrons according to equation 4. The trapped electrons are released back to the conduction band and recombine with the holes in the surface region, leading to the hole accumulation layer becoming thinner and thereby increasing the resistance of the Co_3O_4 nanoparticle. On the other hand, for the TiO_2 nanoparticle, xylene molecules are adsorbed onto the surface of TiO_2 nanoparticle and also react with the adsorbed oxygen species (O_2^-(ads)) on the surface, forming CO_2 and H_2O and releasing free electrons according to

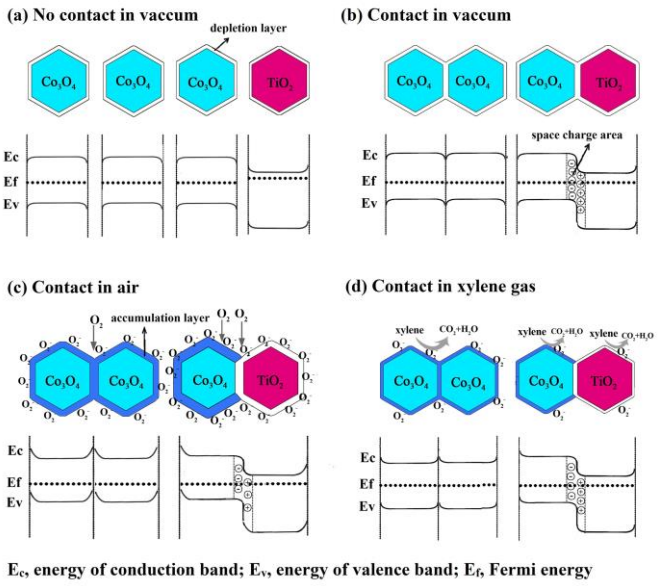

Fig. 9 The schematic diagram of the proposed sensing mechanism and energy band structure diagram of pure Co_3O_4 and CoTiO–4–350 gas sensors.

equation 4,[51] which results in an increase of the carrier concentration in TiO_2 nanoparticle and a decrease of the electron depletion thickness. In other words, the release of electrons decreases the resistance of TiO_2 nanoparticle.

$$2\ C_8H_{10}\ (ads) + 21\ O_2^-(ads) \rightarrow 16\ CO_2\ (g) + 10\ H_2O\ (g) + 21\ e^- \quad (4)$$

According to above analysis, the behavior of Co_3O_4 and TiO_2 is contrary to each other. The total change in the resistance of Co_3O_4–TiO_2 p–n heterojunction during the sensing process might be smaller than that of Co_3O_4–Co_3O_4 p–p homojunction because the behavior of Co_3O_4 and TiO_2 go against with each other, which must be disadvantageous to the sensitivity of Co_3O_4–TiO_2 p–n heterojunction towards xylene. Nevertheless, the adverse effect is significantly overcome by the favorable effect of the Co_3O_4–TiO_2 p–n heterojunction on the sensitivity. There are lots of Co_3O_4–TiO_2 p–n heterojunctions, Co_3O_4–Co_3O_4 p–p homojunctions and some TiO_2–TiO_2 n–n homojunctions in CoTiO–4 nanocomposites. In fact, the TiO_2–TiO_2 n–n homojunctions play a little role on the response to xylene gas because of their low activity and expected relatively small amount in the CoTiO–4 nanocomposites, whereas Co_3O_4–TiO_2 p–n heterojunctions play a crucial role on the sensing performance of the sensor due to the prominent gas adsorption ability of p–n heterojunctions. It has been reported that oxygen and testing gases are much easier to be adsorbed onto the surface of heterojunction than the homojunction.[52] Therefore, more oxygen is adsorbed onto the surface of Co_3O_4–TiO_2 p–n heterojunction than that of Co_3O_4–Co_3O_4 p–p homojunction, which has been proved by the XPS analysis.

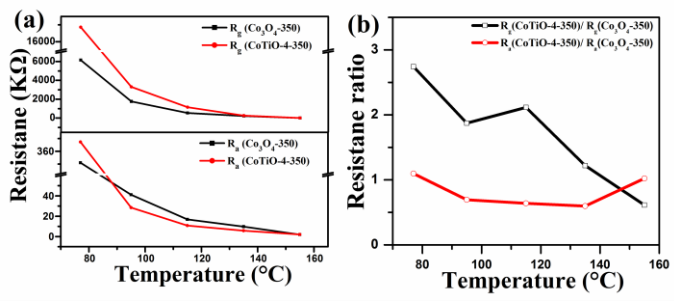

Fig. 10 (a) The resistance changes of Co_3O_4–350 and CoTiO–4–350, and (b) the resistance ratio of CoTiO–4–350 to Co_3O_4–350 in air and 50 ppm xylene at different temperatures.

Actually, as shown in Fig. 10a, b and Table S3 in the supporting information, the R_a of CoTiO–4–350 is larger than that of Co_3O_4–350 at 77 °C due to the self-built electric field in Co_3O_4–TiO_2 p–n heterojunction, which hinders the flow of holes from Co_3O_4 nanoparticle to TiO_2 nanoparticle. However,the R_a of CoTiO–4–350 is much lower than that of Co_3O_4–350 when the temperature was elevated to 95–135 °C, indicating that much more O_2^-(ads) ions are formed on the surface of Co_3O_4–TiO_2 p–n heterojunction and more holes are generated in the surface region of Co_3O_4–TiO_2 p–n heterojunction than that of Co_3O_4–350, resulting from its larger specific surface area and easy formation of O_2^-(ads) on surface of Co_3O_4–TiO_2 p–n heterojunction. Upon exposure to xylene, in comparison with Co_3O_4–350, more xylene molecules will be adsorbed onto the the surface of Co_3O_4–TiO_2 p–n heterojunction and react with the reactive O_2^-(ads) ions. The hole accumulation layer of CoTiO–4–350 will thereby become much thinner than that of Co_3O_4–350 because more electrons are released back to combine with holes in CoTiO–4–350. In addition, the self-built electric field in Co_3O_4–TiO_2 p–n heterojunction will further increase the resistance of CoTiO–4–350, leading to a much higher R_g of CoTiO–4–350 than that of Co_3O_4–350, which agrees well with the results obtained in this study.

In short, in comparison with the pure Co_3O_4 nanoparticle, the formation of p–n heterojunctions in the Co_3O_4–TiO_2 nanocomposites greatly decreases the resistance in air and increases the resistance in xylene gas at 115 °C. According to the definition of response (R_g/R_a), the enhanced response to xylene can be ascribed to the larger change in resistance caused by the formation of p–n heterojunctions in addition to its larger specific surface area. According to previous reports,[53-55] the formation of p–n heterojunctions can form self-built electric field and adsorb more gas molecules, which is especially in favor of improving the sensing performance, giving good explanation to the results obtained in this study.

Conclusions

In summary, mesoporous hierarchical Co_3O_4–TiO_2 p–n heterojunctions have been synthesized by calcining CoTi–LDH precursors prepared through a facile co-precipitation method at suitable temperature. The structure and morphology of Co_3O_4–TiO_2 nanocomposites were characterized by XRD, SEM, TEM, HRTEM and XPS, which confirms the successful formation of p–n heterojunctions. The Co_3O_4–TiO_2 p–n heterojunctions with a Co/Ti molar ratio of 4 show significantly improved xylene and toluene sensing response at low temperature, which is about a 3.5–fold and 2.5–fold increase in comparison with that of the pristine Co_3O_4, respectively. The marked enhancement could be attributed to the hierarchical structure, high specific surface area, and the formation of abundant p–n heterojunctions, leading to full exposure of active sites, easy adsorption of oxygen and target gases, and large modulation of resistance. Moreover, the hierarchical Co_3O_4–TiO_2 p–n heterojunctions also show good selectivity and long-term durability, which is vital for their practical application as well. Therefore, the hierarchical Co_3O_4–TiO_2 p–n heterojunctions are promising candidate in the field of gas sensing, and the combination of hierarchical structure and p–n heterojunctions is an efficient strategy to prepare high-performance gas sensing materials.

Acknowledgements

This work was supported by the National Natural Science Foundations of China (21371022, U1507119), National Key Research and Development Program of China (2016YFB0301601, 2016YFB0301602), National Major Scientific Instruments Development Project of China (21627813), and the Fundamental Research Funds for the Central Universities (YS1406). Pinggui Tang particularly appreciates the aids of China Scholarship Council.

Notes and references

1 H. Nguyen and S. A. El-Safty, *J. Phys. Chem. C*, 2011, **115**, 8466-8474.
2 S. Deng, N. Chen, D. Deng, Y. Li, X. Xing and Y. Wang, *Ceram. Int.*, 2015, **41**, 11004-11012.
3 H. M. Jeong, J. H. Kim, S. Y. Jeong, C. H. Kwak and J. H. Lee, *ACS Appl. Mater. Interfaces*, 2016, **8**, 7877-7883.
4 M. R. Alenezi, S. J. Henley, N. G. Emerson and S. R. P. Silva, *Nanoscale*, 2014, **6**, 235-247.
5 L. Zu, Y. Qin and J. Yang, *J. Mater. Chem. A*, 2015, **3**, 10209-10218.
6 X. Zhou, Y. Zhu, W. Luo, Y. Ren, P. Xu, A. A. Elzatahry, X. Cheng, A. Alghamdi, Y. Deng and D. Zhao, *J. Mater. Chem. A*, 2016, **4**, 15064-15071.
7 J. Liu, M. Dai, T. Wang, P. Sun, X. Liang, G. Lu, K. Shimanoe and N. Yamazoe, *ACS Appl. Mater. Interfaces*, 2016, **8**, 6669-6677.
8 Y. Bing, Y. Zeng, C. Liu, L. Qiao and W. Zheng, *Nanoscale*, 2015, **7**, 3276-3284.
9 H.-R. Kim, A. Haensch, I.-D. Kim, N. Barsan, U. Weimar and J.-H. Lee, *Adv. Funct. Mater.*, 2011, **21**, 4456-4463.
10 S. Wang, B. Xiao, T. Yang, P. Wang, C. Xiao, Z. Li, R. Zhao and M. Zhang, *J. Mater. Chem. A*, 2014, **2**, 6598.

11 S. Xu, J. Gao, L. Wang, K. Kan, Y. Xie, P. Shen, L. Li and K. Shi, *Nanoscale*, 2015, **7**, 14643-14651.
12 L. Jia and W. Cai, *Adv. Funct. Mater.*, 2010, **20**, 3765-3773.
13 C. Sun, X. Su, F. Xiao, C. Niu and J. Wang, *Sens. Actuators, B*, 2011, **157**, 681-685.
14 H.-M. Jeong, H.-J. Kim, P. Rai, J.-W. Yoon and J.-H. Lee, *Sens. Actuators, B*, 2014, **201**, 482-489.
15 Z. Wen, L. Zhu, W. Mei, Y. Li, L. Hu, L. Sun, W. Wan and Z. Ye, *J. Mater. Chem. A*, 2013, **1**, 7511-7518.
16 J. Deng, L. Wang, Z. Lou and T. Zhang, *J. Mater. Chem. A*, 2014, **2**, 9030.
17 E. Şennik, O. Alev and Z. Z. Öztürk, *Sens. Actuators, B*, 2016, **229**, 692-700.
18 N. A. Isaac, M. Valenti, A. Schmidt-Ott and G. Biskos, *ACS Appl. Mater. Interfaces*, 2016, **8**, 3933-3939.
19 S.-J. Choi, S. Chattopadhyay, J. J. Kim, S.-J. Kim, H. L. Tuller, G. C. Rutledge and I.-D. Kim, *Nanoscale*, 2016, **8**, 9159-9166.
20 Y. Li, W. Luo, N. Qin, J. Dong, J. Wei, W. Li, S. Feng, J. Chen, J. Xu, A. A. Elzatahry, M. H. Es-Saheb, Y. Deng and D. Zhao, *Angew. Chem. Int. Ed.*, 2014, **53**, 9035-9040.
21 S. Vallejos, P. Umek, T. Stoycheva, F. Annanouch, E. Llobet, X. Correig, P. De Marco, C. Bittencourt and C. Blackman, *Adv. Funct. Mater.*, 2013, **23**, 1313-1322.
22 L. Sun, X. Han, K. Liu, S. Yin, Q. Chen, Q. Kuang, X. Han, Z. Xie and C. Wang, *Nanoscale*, 2015, **7**, 9416-9420.
23 Y. V. Kaneti, Q. M. D. Zakaria, Z. Zhang, C. Chen, J. Yue, M. Liu, X. Jiang and A. Yu, *J. Mater. Chem. A*, 2014, **2**, 13283-13292.
24 S. Yan and Q. Wu, *J. Mater. Chem. A*, 2015, **3**, 5982-5990.
25 X. Wan, J. Wang, L. Zhu and J. Tang, *J. Mater. Chem. A*, 2014, **2**, 13641-13647.
26 D. P. Volanti, A. A. Felix, M. O. Orlandi, G. Whitfield, D.-J. Yang, E. Longo, H. L. Tuller and J. A. Varela, *Adv. Funct. Mater.*, 2013, **23**, 1759-1766.
27 D. Ju, H. Xu, Z. Qiu, J. Guo, J. Zhang and B. Cao, *Sens. Actuators, B*, 2014, **200**, 288-296.
28 Y. Lu, W. Zhan, Y. He, Y. Wang, X. Kong, Q. Kuang, Z. Xie and L. Zheng, *ACS Appl. Mater. Interfaces*, 2014, **6**, 4186-4195.
29 Y. Liu, H. Dai, J. Deng, S. Xie, H. Yang, W. Tan, W. Han, Y. Jiang and G. Guo, *J. Catal.*, 2014, **309**, 408-418.
30 H. Wu, L. Wang, Z. Shen and J. Zhao, *J. Mol. Catal. A-Chem.*, 2011, **351**, 188-195.
31 H.-S. Woo, C.-H. Kwak, J.-H. Chung and J.-H. Lee, *Sens. Actuators, B*, 2015, **216**, 358-366.
32 M. Hübner, C. E. Simion, A. Tomescu-Stănoiu, S. Pokhrel, N. Bârsan and U. Weimar, *Sens. Actuators, B*, 2011, **153**, 347-353.
33 L. Wang, J. Deng, Z. Lou and T. Zhang, *Sens. Actuators, B*, 2014, **201**, 1-6.
34 F. E. Annanouch, Z. Haddi, M. Ling, F. Di Maggio, S. Vallejos, T. Vilic, Y. Zhu, T. Shujah, P. Umek, C. Bittencourt, C. Blackman and E. Llobet, *ACS Appl. Mater. Interfaces*, 2016, **8**, 10413-10421.
35 S. Park, S. Kim, H. Kheel and C. Lee, *Sens. Actuators, B*, 2016, **222**, 1193-1200.
36 E. M. Seftel, M. C. Puscasu, M. Mertens, P. Cool and G. Carja, *Appl. Catal. B- Environ.*, 2014, **150-151**, 157-166.
37 M. Shao, J. Han, M. Wei, D. G. Evans and X. Duan, *Chem. Eng. J.*, 2011, **168**, 519-524.
38 J. Feng, C. Ma, P. J. Miedziak, J. K. Edwards, G. L. Brett, D. Li, Y. Du, D. J. Morgan and G. J. Hutchings, *Dalton Trans.*, 2013, **42**, 14498-14508.
39 F. Song and X. Hu, *J. Am. Chem. Soc.*, 2014, **136**, 16481-16484.
40 X. Cai, X. Shen, L. Ma, Z. Ji, C. Xu and A. Yuan, *Chem. Eng. J.*, 2015, **268**, 251-259.
41 M.-Y. Guan, D.-M. Xu, Y.-F. Song and Y. Guo, *Sens. Actuators, B*, 2013, **188**, 1148-1154.
42 Y. Ge, K. Kan, Y. Yang, L. Zhou, L. Jing, P. Shen, L. Li and K. Shi, *J. Mater. Chem. A*, 2014, **2**, 4961.
43 Q.-H. Xu, D.-M. Xu, M.-Y. Guan, Y. Guo, Q. Qi and G.-D. Li, *Sens. Actuators, B*, 2013, **177**, 1134-1141.
44 L. Zhang, Z. Gao, C. Liu, Y. Zhang, Z. Tu, X. Yang, F. Yang, Z. Wen, L. Zhu, R. Liu, Y. Li and L. Cui, *J. Mater. Chem. A*, 2015, **3**, 2794-2801.
45 F. Qu, C. Feng, C. Li, W. Li, S. Wen, S. Ruan and H. Zhang, *Int. J. Appl. Ceram. Tec.*, 2014, **11**, 619-625.
46 H. Sun, Z. Chu, D. Hong, G. Zhang, Y. Xie, L. Li and K. Shi, *J. Alloys Compd.*, 2016, **658**, 561-568.
47 F. Qu, Y. Wang, Y. Wang, J. Zhou and S. Ruan, *RSC Adv.*, 2014, **4**, 24211.
48 Y. Li, X. Ma, S. Guo, B. Wang, D. Sun, X. Zhang and S. Ruan, *RSC Adv.*, 2016, **6**, 22889-22895.
49 S. Liu, Z. Wang, H. Zhao, T. Fei and T. Zhang, *Sens. Actuators, B*, 2014, **197**, 342-349.
50 L. Wang, J. Deng, Z. Lou and T. Zhang, *J. Mater. Chem. A*, 2014, **2**, 10022.
51 N. Chen, D. Deng, Y. Li, X. Xing, X. Liu, X. Xiao and Y. Wang, *RSC Adv.*, 2016, **6**, 49692-49701.
52 D. R. Miller, S. A. Akbar and P. A. Morris, *Sens. Actuators, B*, 2014, **204**, 250-272.
53 M. W. Hoffmann, L. Mayrhofer, O. Casals, L. Caccamo, F. Hernandez-Ramirez, G. Lilienkamp, W. Daum, M. Moseler, A. Waag, H. Shen and J. D. Prades, *Adv. Mater.*, 2014, **26**, 8017-8022.
54 S. Bai, H. Liu, R. Luo, A. Chen and D. Li, *RSC Adv.*, 2014, **4**, 62862-62868.
55 Y. Q. Liang, Z. D. Cui, S. L. Zhu, Z. Y. Li, X. J. Yang, Y. J. Chen and J. M. Ma, *Nanoscale*, 2013, **5**, 10916-10926.